ZIRCONIUM EFFECT ON THE CORROSION BEHAVIOR OF 316L STAINLESS STEEL ALLOY AND HASTELLOY-N SUPERALLOY IN MOLTEN FLUORIDE SALT

MATERIALS FOR NUCLEAR SYSTEMS

KEYWORDS: *molten fluoride salt, coating, galvanic effect*

WEI-JEN CHENG,[a,b] ROBERT S. SELLERS,[a] MARK H. ANDERSON,[a] KUMAR SRIDHARAN,[a]* CHAUR-JENG WANG,[b] and TODD R. ALLEN[a]

[a]*University of Wisconsin–Madison, Department of Engineering Physics*
1500 Engineering Drive, Madison, Wisconsin 53711
[b]*National Taiwan University of Science and Technology*
Department of Mechanical Engineering, Taipei 10607, Taiwan

Received August 8, 2012
Accepted for Publication December 4, 2012

A corrosion test was performed on 316L stainless steel alloy (316L) and Hastelloy-N superalloy (Hastelloy-N) at 850°C for 1000 h in static molten fluoride salt, 46.5LiF-11.5NaF-42KF (mol %) with Zr additions. The interactions between the graphite sample and the tested alloys in the molten salt were also analyzed. The results show that Zr addition to the salt caused the deposition of a pure Zr coating on 316L and Hastelloy-N. The formation of this coating was followed by interdiffusion between the Zr deposit and the substrates. A thicker Zr deposit was observed on Hastelloy-N samples compared to 316L due to the larger electromotive potential difference between Ni/Zr than that between Fe/Zr. The interdiffusion subsequent to Zr deposition led to the formation of a coating composed of a Ni/Zr intermetallic phase even on the iron-based 316L. This intermetallic coating on the two alloys acted as a barrier layer for Fe and Cr outward diffusion. Zr_3NiO and ZrO_2 phases were also observed on the coating surfaces and in the coatings, respectively. The graphite sample, on the other hand, had no direct and significant effect on the corrosion behavior of the alloys and the coating formation on the alloys.

I. INTRODUCTION

Molten fluoride salts have been proposed for use as primary and secondary coolants for a Fluoride Salt–Cooled High-Temperature Reactor (FHR) and as a medium for heat transfer for nuclear cogeneration in the very high temperature reactor[1,2] (VHTR). A eutectic fluoride salt with composition of 46.5LiF-11.5NaF-42KF (mol %), commonly referred to as FLiNaK, has been suggested as one of the candidate fluoride salts because of its favorable characteristics such as low melting point, high boiling point, low viscosity, high heat capacity, and thermal conductivity.[1,2] However, the issue of materials corrosion in molten fluoride salts, particularly at high temperatures, has been raised in previous studies[3–5] and must be addressed before these salts are used in the aforementioned advanced reactor concepts.

Three corrosion mechanisms of materials in static molten fluoride salts have been proposed: intrinsic corrosion, corrosion by impurities, and galvanic corrosion.[6] Intrinsic corrosion is driven by the free energy of formation of transition metal fluorides. A more negative formation free energy indicates that the transition metal fluoride is more stable in fluoride salts. Based on this criterion, we rank the corrosion resistance of the common metallic alloying elements to molten fluoride salt (from low to high) as follows: Al, Zr, Ti, Mn, Cr, Nb, Fe, Co, Ni, Mo, and W (Ref. 3). Impurities in molten fluoride salts can dramatically increase the corrosion of materials. H_2O is the most common impurity in FLiNaK due to

*E-mail: kumars@cae.wisc.edu

the hygroscopic nature of one of its constituents: KF. H_2O-induced corrosion includes the following reactions of HF generation [Eqs. (1) and (2)]:

$$H_2O + 2F^- \leftrightarrow O^{2-} + 2HF \quad (1)$$

and

$$H_2O + F^- \leftrightarrow OH^- + HF \quad (2)$$

and the following reaction of corrosion of the metal by HF [Eq. (3)] (Ref. 4):

$$M^0 + x\mathrm{HF} \leftrightarrow x/2\mathrm{H}_2 + \mathrm{MF}_x \ , \quad (3)$$

where M = Ni, Fe, Cr, etc.

Galvanic corrosion occurs when metals with differing electromotive potentials (EMPs) are in electrical contact in molten fluoride salts. In a galvanic couple, the metal with the more negative EMP tends to act anodically while the metal with the more positive EMP tends to act cathodically. Thus, material corrosion in molten fluoride salts is accelerated due to the oxidation reaction at the anodic component.[4]

The 316L stainless steel Fe-Ni-Cr iron-based alloy (316L) has been widely used for components and structural materials in the current-generation nuclear power plants because of its excellent high-temperature creep strength, corrosion resistance, and sensitization resistance.[7] On the other hand, the Hastelloy-N Ni-Mo-Cr nickel-based superalloy (Hastelloy-N) has been developed by Oak Ridge National Laboratory (ORNL) specifically for use in the Molten Salt Reactor (MSR) Experiment.[8,9] The Ni and high Mo contents in Hastelloy-N provide excellent resistance to the molten fluoride salt corrosion.[10] Previous studies on materials corrosion in static molten fluoride salt have shown that alloys with high Ni and low Cr contents exhibit better corrosion resistance.[6] Based on this result, we believe that Hastelloy-N should have superior resistance to the molten fluoride salt than 316L.

Studies dealing with molten salt chemistry have shown that control of oxidation-reduction potential is an effective method to restrain the corrosion of a material in the molten salt.[11–14] This technique uses a sacrificial material, the reductant, to maintain a reducing environment in the molten salt. In an ORNL study concerning redox control of molten fluoride salts,[11] Zr has been recognized as a strong reductant; 4700 parts per million (ppm) of Cr was reduced from molten 66LiF-34BeF (mol %) salt by ~6400 ppm Zr addition. Unfortunately, prevention of corrosion of structural materials in molten fluoride salts by the use of reductant addition for redox control has not been thoroughly investigated.

The purpose of this research is to study the effect of Zr addition, as a redox control agent, on the corrosion behavior of 316L and Hastelloy-N in molten fluoride salt. Corrosion tests on 316L and Hastelloy-N were performed at 850°C for 1000 h in molten FLiNaK salt. Graphite samples were introduced to the corrosion test to study the interaction among the alloys, graphite, and Zr in molten FLiNaK salt. This was done because graphite has been incorporated in several reactor designs: as a component of the reactor core in the MSR and as the shell for TRISO fuel particles in the advanced high temperature reactor (AHTR).

II. EXPERIMENTAL

Commercial 316L and Hastelloy-N were used in this study. The chemical compositions of the alloys are shown in Table I. A laser was used to cut 316L samples to the dimensions of 25 × 13 × 1 mm. Hastelloy-N samples from stock were milled to the same size. The graphite samples were milled to have approximately twice the surface area of a single metallic sample. The purified graphite was procured from POCO, grade AFX-5Q with an average particle size of 5 μm and an average pore size of 0.8 μm. The surface area of each alloy coupon and the alloy vessel were 6.5 and 237 cm^2, respectively. Two diagonally opposing holes were drilled in the samples for attaching to the sample rods by 316L wire. The 316L and Hastelloy-N samples were then ground with SiC paper to a 1200-grit finish. To remove the contamination from the surface of the samples, we ultrasonically cleaned samples in ethanol and deionized water and then dried them in air. FLiNaK used for the

TABLE I

Chemical Compositions of Alloys Used in This Study*

Alloy	C	Fe	Ni	Mn	Si	Cr	Mo	P	S
316L	0.02	[a]	10.27	1.64	0.52	17.23	2.22	0.03	0.02
Hastelloy-N	0.08[b]	4.12	[a]	0.80	1.50	8.00	16.19	—	—

*In units of weight percent.
[a]As balance.
[b]Maximum.

corrosion test was produced in a glove box under argon atmosphere. Pure LiF, NaF, and KF were mixed according to the ratio of FLiNaK in a SiC crucible. The SiC crucible containing the salt was heated to 700°C for 3 days and then cooled down to room temperature to produce homogeneous FLiNaK. The produced FLiNaK was broken into small pieces for the corrosion test.

The corrosion test was performed in a sealed, welded-shut crucible with a sample rod installed at its center. A schematic of the test system can be seen in Fig. 1a. All crucible components were made of 316L. We placed 513 ± 2.5 g of broken-up salt and 10 g of pure Zr rod into each crucible. The pure Zr rod was on the bottom of the crucible. The crucibles were welded shut in an argon-atmosphere glove box. Four crucibles were used for the corrosion test, which were designated as 6-Zr, 6-Zr-Gr, N-Zr, and N-Zr-Gr, where "6," "N," "Zr," and "Gr" represent 316L, Hastelloy-N, zirconium, and graphite, respectively. Each crucible contained three samples. The sample combination in each crucible is shown in Table II.

After 1000 h, the temperature of the furnace was decreased for several hours to 550°C, which is ~100°C above the melting point of FLiNaK. This temperature was selected to ensure that the salt would still be liquid while reducing safety issues associated with opening a hot furnace. The crucibles were removed from the furnace, flipped upside down, and allowed to cool to room temperature. This technique prevents frozen salt from coming into contact with samples in order to make the removal of samples easier. The crucibles were cut open using an abrasive disk handsaw, and the samples were retrieved. To remove the residual salt on the samples, we ultrasonically cleaned the retrieved samples in 1 *M* $Al(NO_3)_3$ solution. The extent of corrosion of the samples was evaluated using weight change measurement. Characterization of the plan-view and cross-sectional morphologies of the samples was carried out by scanning electron microscopy (SEM) with energy dispersive spectrometry (EDS) and X-ray diffraction (XRD).

III. RESULTS

III.A. Weight Change of 316L and Hastelloy-N

Figure 1b shows the weight change results of the 316L and Hastelloy-N samples after corrosion. All of the samples gained weight after the corrosion tests except the graphite samples in the 6-Zr-Gr and N-Zr-Gr crucibles (see Table II). Both graphite samples were corroded and broken into small pieces in the molten salt. The weight gain of the 316L and Hastelloy-N samples indicates surface material deposition. The Hastelloy-N samples had a larger weight gain than the 316L samples.

III.B. Microstructure and Phase Constitution of Coatings on 316L

The plan-view and cross-sectional SEM micrographs of the 316L samples after corrosion are shown in Fig. 2. Both 6-Zr and 6-Zr-Gr samples exhibited a multiphase coating layer. The thickness of the coating on the 6-Zr sample was twice that of the 6-Zr-Gr sample, being ~12 μm and ~6 μm, respectively. From the top-view SEM micrographs, it can be observed that the surface of the coating on the 6-Zr sample had a dense structure, while the surface of the coating on the 6-Zr-Gr sample

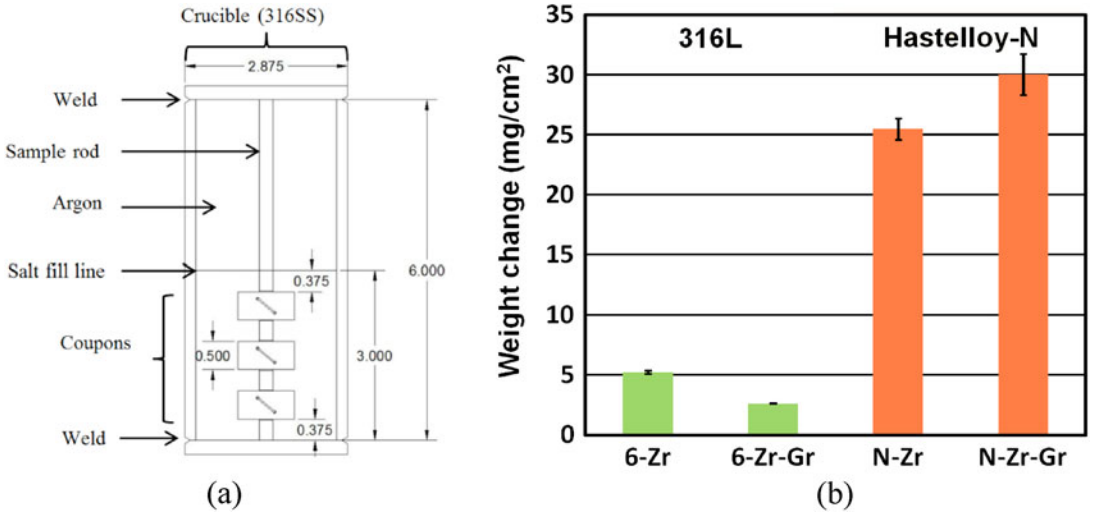

Fig. 1. (a) Schematic view of the static corrosion test crucible. All crucible materials are made of 316L. All measurements are in inches. The coupons are attached to the sample rod by 316L wire. (b) Weight change of 316L and Hastelloy-N samples exposed to molten FLiNaK salt at 850°C for 1000 h. Graphite samples not weighed because of breaking during exposure.

TABLE II

Test Matrix Used in This Study

	Crucible Label[a]			
	6-Zr	6-Zr-Gr	N-Zr	N-Zr-Gr
Crucible material	316L	316L	316L	316L
Sample 1	316L	316L	Hastelloy-N	Hastelloy-N
Sample 2	316L	Graphite	Hastelloy-N	Graphite
Sample 3	316L	316L	Hastelloy-N	Hastelloy-N
Redox control	Zirconium	Zirconium	Zirconium	Zirconium

[a]The "6," "N," "Zr," and "Gr" used to label the crucible represent 316L, Hastelloy-N, zirconium, and graphite, respectively.

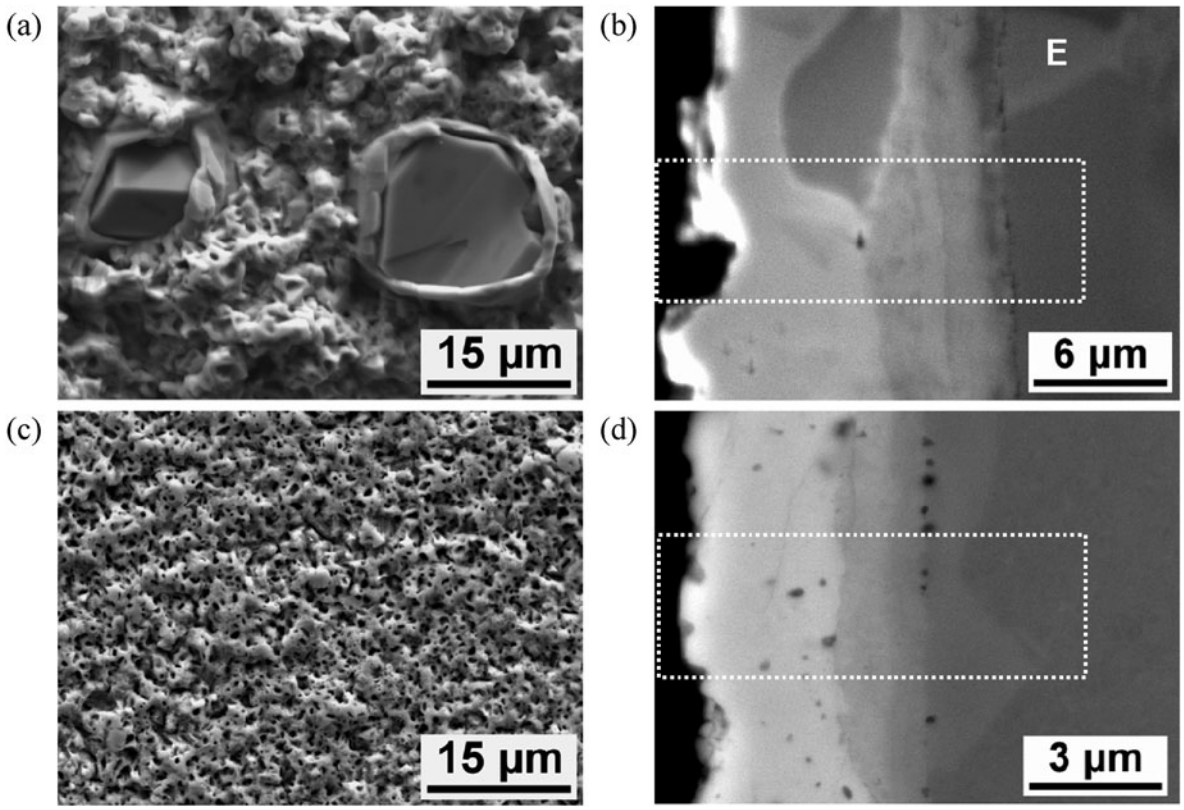

Fig. 2. (a) SEM top-view micrograph of 6-Zr sample, (b) SEM cross-sectional micrograph of 6-Zr sample, (c) SEM top-view micrograph of 6-Zr-Gr sample, and (d) SEM cross-sectional micrograph of 6-Zr-Gr sample—all exposed to molten FLiNaK salt at 850°C for 1000 h.

possessed a porous structure. Some crystals were observed to be embedded in the coating only for the 6-Zr samples. Figure 3 shows the XRD results of the coating surfaces on the 6-Zr and 6-Zr-Gr samples; Zr_3NiO and $NiZr_2$ were identified on both samples, while ZrO_2 existed on only the 6-Zr samples.

To determine the elemental distribution in the coating, we performed EDS X-ray mapping on a selected rectangular area on the cross-sectional SEM micrograph, as shown in Fig. 4. The coatings on 6-Zr and 6-Zr-Gr exhibited similar elemental distribution characteristics, being comprised primarily of Zr and Ni. The major constituents of 316L, Fe and Cr, could be found only at the inner part of the coating. On the other hand, the X-ray mapping results also revealed the locations of the phases with different chemical compositions in the coating. To understand the phase constitution of the coating, we further identified the phases exposed by the X-ray mapping

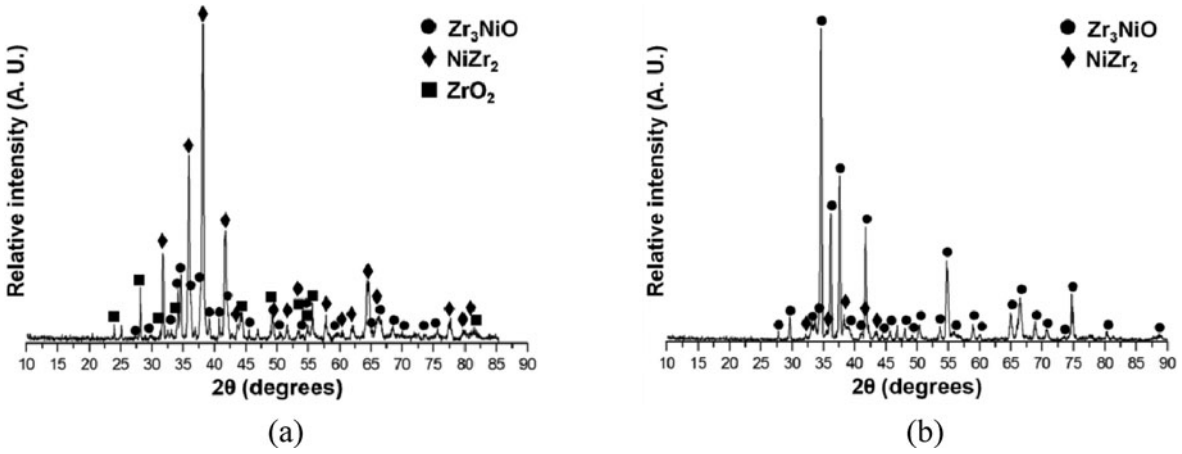

Fig. 3. XRD analysis of coating surfaces on (a) 6-Zr and (b) 6-Zr-Gr samples exposed to molten FLiNaK salt at 850°C for 1000 h.

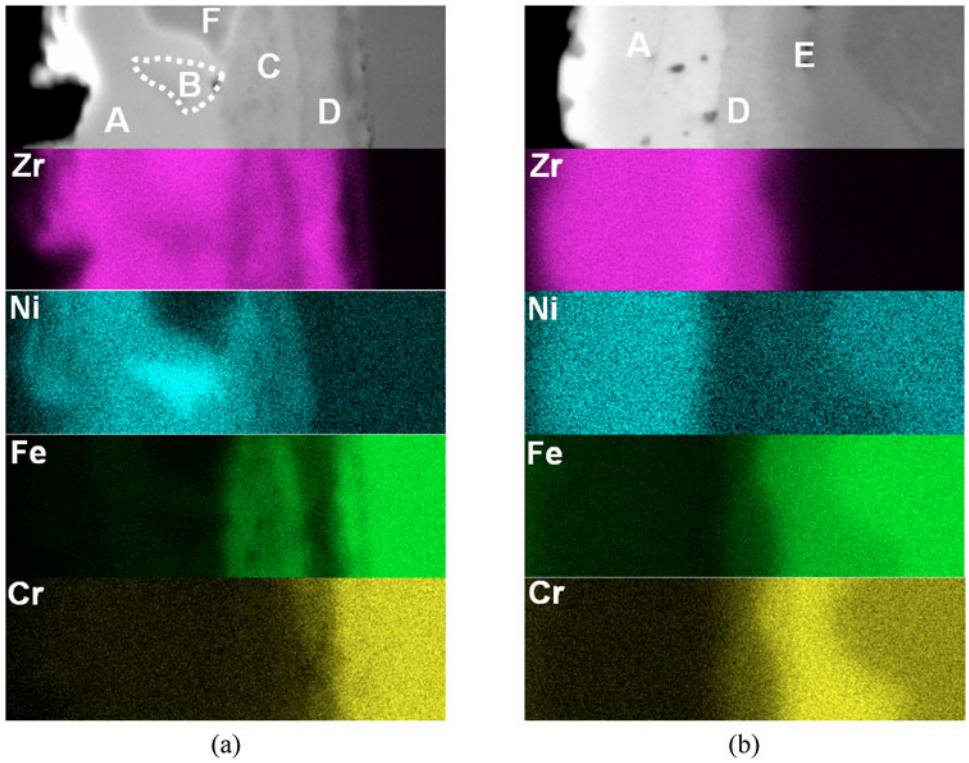

Fig. 4. SEM cross-sectional micrographs and corresponding EDS X-ray mapping of (a) 6-Zr and (b) 6-Zr-Gr samples exposed to molten FLiNaK salt at 850°C for 1000 h. The observation areas are the dotted rectangular regions in Figs. 2b and 2d. Letters "A" through "F" indicate phases with different chemical compositions revealed by EDS X-ray mapping.

by comparing their EDS-measured compositions with the related phase diagrams. The phase identification results are shown in Table III. The coatings on the 6-Zr and 6-Zr-Gr samples mainly comprise outer Ni-Zr binary intermetallic phases and inner Fe-Zr binary intermetallic phases, in which Ni, Fe, and Cr could substitute for each other within a certain solubility of each phase. The embedded crystals found in the coating on the 6-Zr sample were identified as ZrO_2. Figure 5 shows the schematics of the phase constitution of the coatings on the 6-Zr and 6-Zr-Gr samples based on the SEM micrographs and the corresponding EDS compositional results. From the coating surface to the substrate, the coatings on the 6-Zr samples were composed of $(Ni,Fe)Zr_2$, ZrO_2, $(Ni,Fe)Zr$,

TABLE III

Phase Identification Based on EDS Chemical Composition Results of Phases in Coatings on 6-Zr and 6-Zr-Gr Samples Exposed to Molten FLiNaK Salt at 850°C for 1000 h

Sample	Phase	EDS Chemical Composition (at. %)									Identification
		O	Al	Si	Cr	Mn	Fe	Ni	Zr	Mo	
6-Zr	A	—	0.8	0.5	0.6	0.1	7.2	25.5	65.2	—	$(Ni,Fe)Zr_2$
	B	—	0.2	0.4	0.4	—	3.5	45.3	50.2	—	(Ni,Fe)Zr
	C	—	2.4	1.8	3.2	0.6	48.5	8.6	35.1	—	$(Fe,Ni)_2Zr$
	D	—	—	1.8	11.7	0.6	20.4	1.2	62.9	1.4	$(Fe,Cr)Zr_2$
	E[a]	—	0.1	4.0	30.6	1.2	58.0	2.2	0.1	3.8	σ-$(Fe,Ni)_3(Cr,Mo)_2$
	F	62.9	—	—	0.1	—	0.5	0.7	35.8	—	ZrO_2
6-Zr-Gr	A	—	—	0.6	1.1	0.1	9.5	16.0	72.7	—	$(Ni,Fe)Zr_2$
	D	—	—	1.7	12.2	0.7	19.6	1.9	62.6	1.4	$(Fe,Cr)Zr_2$
	E	—	0.1	4.6	30.9	1.2	56.1	3.0	0.9	3.3	σ-$(Fe,Ni)_3(Cr,Mo)_2$

[a]This phase is labeled in Fig. 2b.

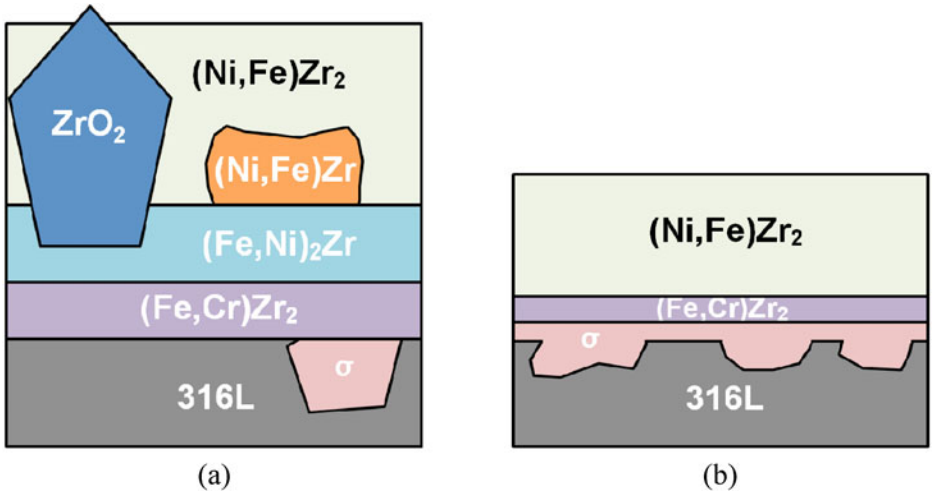

Fig. 5. Schematic configuration of the phase constitution of coatings on (a) 6-Zr and (b) 6-Zr-Gr samples exposed to molten FLiNaK salt at 850°C for 1000 h.

$(Fe,Ni)_2Zr$, $(Fe,Cr)Zr_2$, and σ-$(Fe,Ni)_3(Cr,Mo)_2$, while the coatings on the 6-Zr-Gr samples were composed of $(Ni,Fe)Zr_2$, $(Fe,Cr)Zr_2$, and σ-$(Fe,Ni)_3(Cr,Mo)_2$ (Refs. 15 through 18).

III.C. Microstructure and Phase Constitution of Coatings on Hastelloy-N

Figure 6 displays the plan-view and cross-sectional SEM micrographs of the Hastelloy-N samples after corrosion. Multiphase coatings were found on the N-Zr and N-Zr-Gr samples. The coatings on N-Zr and N-Zr-Gr had similar cross-sectional microstructures as well as thicknesses (~65 μm). A microstructural difference between the coatings on the N-Zr and N-Zr-Gr samples was that the coating on the N-Zr samples exhibited a larger number and size of embedded crystals than the coating on the N-Zr-Gr samples. Also, the top-view SEM micrographs of the coating on the N-Zr and N-Zr-Gr samples revealed that the coating surface of N-Zr had a dense structure, while the coating surface of N-Zr-Gr had a porous structure. The coating surfaces on the N-Zr and N-Zr-Gr samples showed a similar XRD result to the 6-Zr and 6-Zr-Gr samples, in which Zr_3NiO, ZrO_2, and NiZr were identified on the N-Zr samples, while Zr_3NiO and $NiZr_2$ were found on the N-Zr-Gr sample.

The EDS X-ray mapping results of the selected rectangular area on the cross-sectional SEM micrographs of

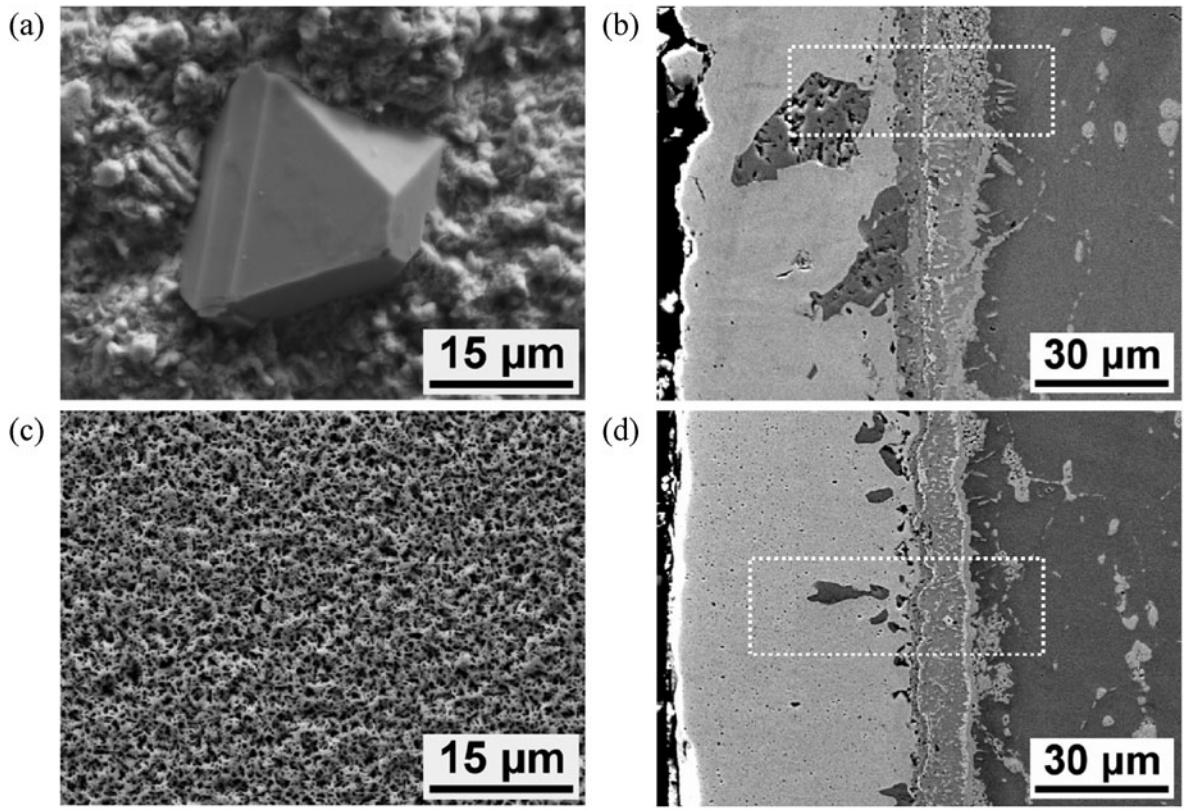

Fig. 6. (a) SEM top-view micrograph of N-Zr sample, (b) SEM cross-sectional micrograph of N-Zr sample, (c) SEM top-view micrograph of N-Zr-Gr sample, and (d) SEM cross-sectional micrograph of N-Zr-Gr sample—all exposed to molten FLiNaK salt at 850°C for 1000 h.

the coatings on N-Zr and N-Zr-Gr are shown in Fig. 7. The coatings on N-Zr and N-Zr-Gr possessed similar element distribution characteristics, being composed of mainly Zr and Ni. In the inner part of the coatings on N-Zr and N-Zr-Gr, the concentrations of Mo and Cr, the second and third major alloying elements in Hastelloy-N, respectively, were higher than their nominal concentrations in the substrate. On the other hand, Al and Si element distribution maps revealed that an Al-rich layer and a Si-rich layer formed above the Mo- and Cr-rich phase in the coating on N-Zr, and a Si-rich layer formed above the Mo- and Cr-rich phase in the coating on N-Zr-Gr.

The phase identification results based on the EDS-measured compositions of the phases in the coatings on N-Zr and N-Zr-Gr are shown in Table IV. The coatings on N-Zr and N-Zr-Gr had a similar phase constitution. Figure 8 shows the schematic illustrations of the phase constitution of the coatings on the N-Zr and N-Zr-Gr samples based on the SEM micrographs and the corresponding EDS compositional results. Figure 8 shows the major phases in the coatings on N-Zr and N-Zr-Gr to be Ni-Zr binary intermetallic phases. The distribution of the Ni-Zr phases from the coating surface to substrate is $NiZr_2$, NiZr, $Ni_{10}Zr_7$, and Ni_7Zr_2, respectively. Among these Ni-Zr phases, the $NiZr_2$ phase formed only in the coating on N-Zr, while $Ni_{10}Zr_7$ was present only in the coating on N-Zr-Gr. The Mo- and Cr-rich phase observed in the inner part of the coating was identified as a (Mo,Cr) solid solution phase and a σ-$Cr_{0.4}Mo_{0.3}Ni_{0.3}$ ternary intermetallic phase. The Al-rich layer in the coating on N-Zr and the Si-rich layer in the coatings on N-Zr and N-Zr-Gr were confirmed to be Ni_2ZrAl and NiZrSi, respectively. The embedded crystals formed in the coatings on N-Zr and N-Zr-Gr were ZrO_2 (Refs. 17 through 21).

III.D. Substrate Depletion by Coating Formation

The phase constitution analysis of the coatings has shown that the Ni-Zr binary intermetallic phases are the main constituents of the coatings on the 316L and Hastelloy-N substrates. This implies that Ni diffuses outward from the substrate even in Fe-based 316L. Figure 9 shows the Ni line scan profiles of the four sample types starting at the coating surface and extending to the substrate. Figure 9 shows that the coatings lead to the formation of an immediately Ni-depleted zone in the substrate immediately under the coatings. The depth of the Ni-depleted zone can be termed as the substrate depletion,

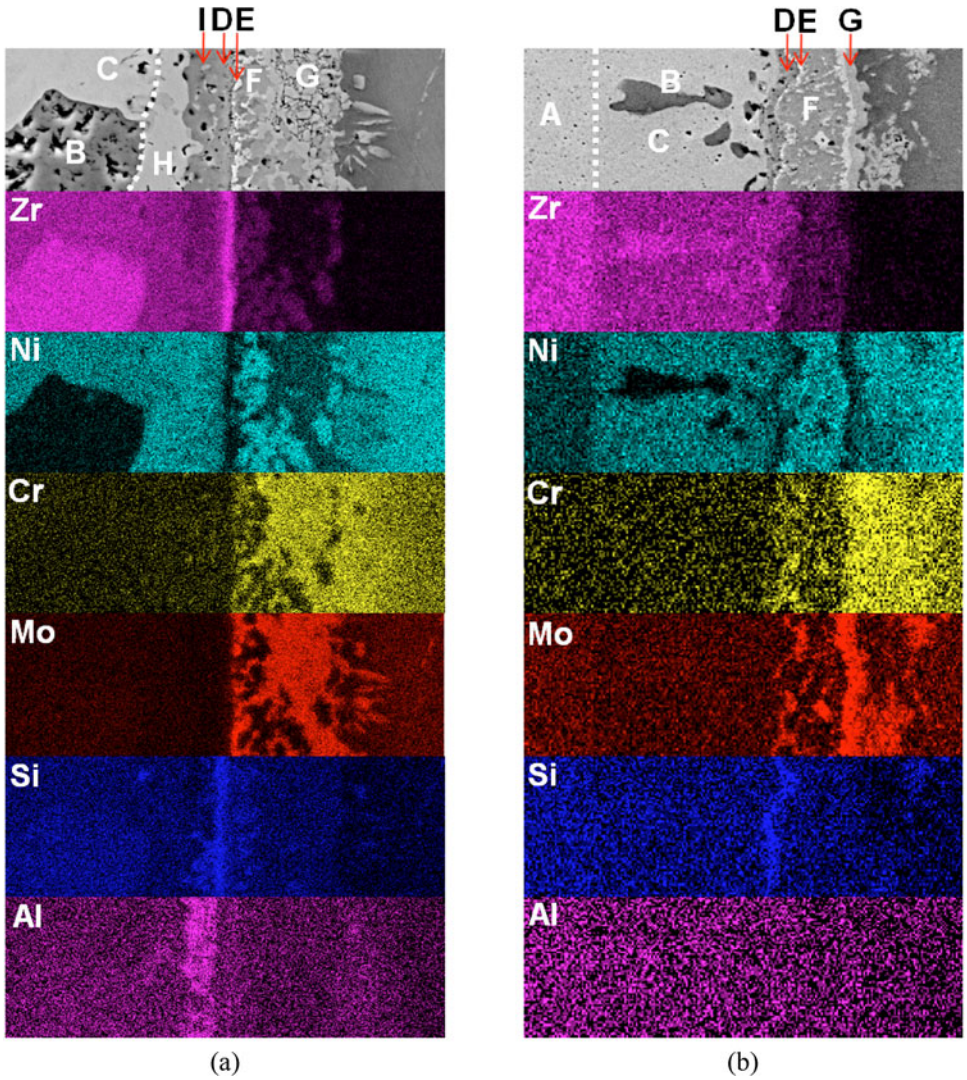

Fig. 7. SEM cross-sectional micrographs and corresponding EDS X-ray mapping of (a) N-Zr and (b) N-Zr-Gr samples exposed to molten FLiNaK salt at 850°C for 1000 h. The observation areas are the dotted rectangular regions in Figs. 6b and 6d. Letters "A" through "I" indicate phases with different chemical compositions revealed by EDS X-ray mapping.

which is the distance between the coating-substrate interface and the remaining good substrate (the substrate containing its nominal composition). The coating thickness and substrate depletion, as well as the weight change, are summarized in Table V. Generally, the Hastelloy-N sample shows relatively larger substrate depletion than the 316L sample. The substrate depletion is proportional to the weight change.

IV. DISCUSSION

This study has shown that Zr addition to molten salts resulted in the formation of a Zr-bearing coating on the surface of the 316L and Hastelloy-N samples. The coatings are composed of Ni-Zr binary intermetallic phases. The Ni in the coating comes from the diffusion of Ni outward from the 316L and Hastelloy-N substrates. Thus, the formation of the coatings occurs by a two-step process involving Zr deposition and then interdiffusion between the Zr coating and the substrates. The results show that the microstructure and phase constitution of the coatings are not only dominated by the Zr addition but also influenced by the graphite sample and the type of substrate. Therefore, the effects of Zr, graphite, and substrate are addressed separately in Secs. IV.A, IV.B, and IV.C.

IV.A. Zirconium Addition Effect

The weight gain and microstructural results of the 316L and Hastelloy-N samples clearly indicate the deposition

TABLE IV

Phase Identification Based on EDS Chemical Composition Results of Phases in Coatings on N-Zr and N-Zr-Gr Samples Exposed to Molten FLiNaK Salt at 850°C for 1000 h

Sample	Phase	EDS Chemical Composition (at. %)									Identification
		O	Al	Si	Cr	Mn	Fe	Ni	Zr	Mo	
N-Zr	B	61.9	—	0.5	—	0.1	0.2	0.6	36.8	—	ZrO_2
	C	—	—	0.5	—	—	0.6	50.0	48.8	—	NiZr
	D	—	1.0	25.8	0.5	0.1	1.9	30.7	40.1	—	NiZrSi
	E	—	0.3	2.3	31.6	0.1	1.4	6.8	4.3	53.2	(Mo,Cr)
	F	—	0.7	4.1	1.6	0.1	1.7	70.1	20.9	0.8	Ni_7Zr_2
	G	—	0.5	4.5	20.7	0.4	8.6	29.4	—	35.9	σ-$Cr_{0.4}Mo_{0.3}Ni_{0.3}$
	H	—	2.6	1.3	0.2	—	0.6	55.4	40.0	—	$Ni_{10}Zr_7$
	I	—	24.4	0.8	0.1	—	0.5	49.2	25.0	—	Ni_2ZrAl
N-Zr-Gr	A	—	—	0.3	0.2	0.1	1.0	24.9	73.5	—	$NiZr_2$
	B	62.5	—	0.4	—	—	0.1	1.5	35.4	—	ZrO_2
	C	—	—	0.5	0.1	—	0.8	48.8	49.9	—	NiZr
	D	—	0.1	25.9	1.1	0.2	2.3	29.4	40.7	0.5	NiZrSi
	E	—	0.1	1.1	26.6	0.3	1.0	3.9	0.7	66.2	(Mo,Cr)
	F	—	0.9	4.6	1.5	0.3	2.2	68.0	22.5	—	Ni_7Zr_2
	G	—	0.3	3.8	20.2	0.5	8.4	30.9	—	35.9	σ-$Cr_{0.4}Mo_{0.3}Ni_{0.3}$

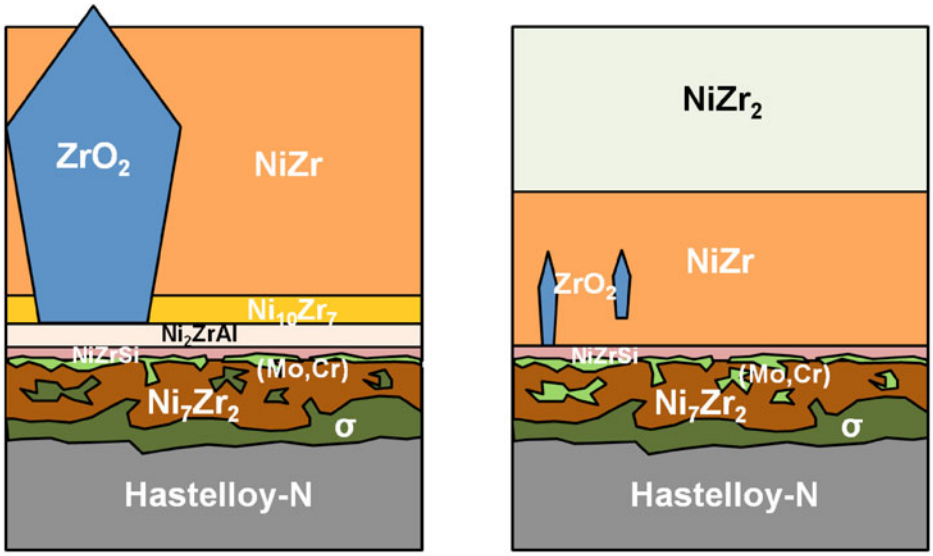

Fig. 8. Schematic configuration of phase constitution of coatings on (a) N-Zr and (b) N-Zr-Gr samples exposed to molten FLiNaK salt at 850°C for 1000 h.

of Zr on the test alloy substrates. Such deposition in the molten salt environments has been addressed by some researchers.[22–24] Kondo et al.[4] studied the corrosion of 8.92Cr-2W ferritic steel (JLF-1) and performed tests of molten FLiNaK salt in crucibles made of JLF-1 and Ni. They found that the Ni crucible accelerated the corrosion of the JLF-1 alloy and enabled plating of Fe corrosion products. Kondo et al. attributed this result to a galvanic effect in which the JLF-1 and the Ni crucible formed the anode and the cathode, respectively, due to Ni being more electropositive than Fe and Cr. The EMPs of the alloy elements versus a Ni reference electrode in FLiNaK at 750°C are −1.25 V for Zr^{4+}/Zr, −0.69 V for Cr^{2+}/Cr, −0.21 V for Fe^{2+}/Fe, and 0 V for Ni^{2+}/Ni (Refs. 24 and 25). In our

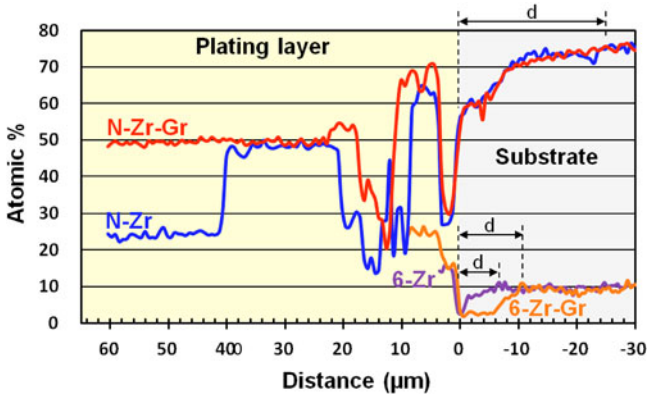

Fig. 9. EDS line scan profiles of Ni starting at the coating surface and extending to the substrate of 316L and Hastelloy-N samples exposed to molten FLiNaK salt at 850°C for 1000 h; "d" indicates the substrate depletion zone.

TABLE V

Summary of Weight Change, Coating Thickness, and Substrate Depletion of 316L and Hastelloy-N Samples Exposed to Molten FLiNaK Salt at 850°C for 1000 h

Sample	Weight Change (mg/cm^2)	Coating Thickness (μm)	Substrate Depletion (μm)
6-Zr	5.23 ± 0.13	12.11 ± 1.51	12.48 ± 2.99
6-Zr-Gr	2.63 ± 0.01	5.98 ± 0.6	8.73 ± 1.68
N-Zr	25.46 ± 0.09	67.15 ± 3.22	18.43 ± 5.50
N-Zr-Gr	30.01 ± 1.70	65.05 ± 4.29	21.42 ± 2.96

study, the Zr ingot and 316L/Hastelloy-N samples also formed galvanic couples, in which Zr acted as the anode while the iron-based and nickel-based samples acted as the cathode. Therefore, an anodic Zr ingot would be oxidized to form a Zr ion in the molten salt, and then the Zr ion was reduced on the cathodic samples. Crystalline ZrO_2 phases were also found to be embedded in the coating. Researchers[26,27] have developed a firm basis for the formation of distinct ZrO_2 phases on material surfaces by electroplating. Although Zr can undergo a variety of reactions in a fluorinating molten salt environment,[23] literature suggests that the ZrO_2 electroplating process must be described by oxidation of Zr [Eq. (4)], hydrolysis of a partial Zr ion [Eq. (5)], and dehydration of the hydroxide [Eq. (6)]:

$$Zr \rightarrow Zr^{4+} + 4e^{-} \quad , \tag{4}$$

$$Zr^{4+} + 4OH^{-} \rightarrow Zr(OH)_4 \quad , \tag{5}$$

and

$$Zr(OH)_4 \rightarrow ZrO_2 + 2H_2O \quad . \tag{6}$$

The source of OH^{-} is likely the H_2O contamination in the salt. It has been reported that KF is a hygroscopic material, which in the case of studies performed by Kondo et al. caused FLiNaK to absorb 16 wt% of H_2O during the process of mixing and melting in air.[4] Zr_3NiO also can be found on all of the coatings' surfaces on 316L and Hastelloy-N, regardless of whether the outer phase of the coatings is NiZr, $NiZr_2$, or $(Ni,Fe)Zr_2$ or if graphite is present in the molten salt. The formation of Zr_3NiO on the coating surfaces not only indicates the oxidation of the coating by H_2O contamination in the salt but also implies that Zr might be able to stabilize the oxide in the molten fluoride salts.

IV.B. Graphite Effect

According to Ozeryanaya et al.'s research of corrosion of Zr in molten chloride salt in glassy carbon crucibles,[28] finely dispersed ZrC particles have been observed in the salt. The formation of ZrC particles is caused by the galvanic interaction between Zr and the glassy carbon crucible, resulting in the transfer of Zr through the molten salt toward the more electropositive glassy carbon crucible. However, the presence of ZrC particles dispersed in the salt implies that the cathodic glassy carbon also dissolves in the galvanic process. Similar results were observed in our study. The graphite samples in the 6-Zr-Gr and N-Zr-Gr crucibles were observed to be dissolved and broken into pieces in the salt even though graphite acted as the cathode in the Zr/graphite galvanic couple. On the other hand, the number and size of the ZrO_2 crystals embedded in the coatings on 316L and Hastelloy-N were much less when graphite was present in the salt. This result can be explained by the dissociation of ZrO_2. The process is as follows:

$$C + 4HF \rightarrow CF_4 + 2H_2 \tag{7}$$

and

$$ZrO_2 + CF_4 \rightarrow ZrF_4 + CO_2 \quad . \tag{8}$$

The graphite sample was initially corroded by HF [Eq. (7)], which was generated by the reaction of H_2O and salt, to form CF_4. The ZrO_2 crystals growing on the sample would be corroded by CF_4 and then generated CO_2 gas [Eq. (8)] (Ref. 29). The porous surface of the coatings on the 6-Zr-Gr and N-Zr-Gr samples could also indicate the formation of gaseous CO_2 released from the dissociation of ZrO_2. Another possible reason for reduced ZrO_2 formation is that the oxygen coming from H_2O contamination was consumed by the formation of CO or CO_2 due to the oxidation of the graphite sample.

IV.C. Substrate Effect

It was observed that the 316L samples had much smaller weight gain and coating thicknesses than the Hastelloy-N samples, indicating that the 316L has less Zr

deposition than Hastelloy-N. This can be explained by the difference of the EMP between the Zr and the iron-based 316L being smaller than the EMP between the Zr and the nickel-based Hastelloy-N (Refs. 24 and 25). The larger difference of EMP in a galvanic couple leads to a higher deposition rate of anodic metal on the cathode. The fact that the coating on 316L is composed of a Ni-Zr intermetallic phase even though 316L is an iron-based alloy, containing 12 wt% Ni, is another result associated with the substrate that needs to be considered. In a companion project,[30] a 316L sample was exposed to FLiNaK using the same conditions as in this study but without any Zr redox agent addition. These tests show that the 316L sample underwent surface depletion of Cr after 1000 h of exposure. This Cr depletion also caused a relative increase in the Fe concentration. The Ni concentration, however, stayed constant with respect to nominal quantity. Based on this result, we surmise that the 316L sample in this study would not form a Ni-rich surface due to the initial Cr depletion, which happened before the Zr deposition. Thus, the coating on the 316L sample would be formed due to the preferential diffusion of Ni instead of Fe into the Zr layer. The evidence for the faster Ni diffusion in Zr is supported by the interdiffusion coefficient of Ni/Zr being four orders of magnitude larger than that of Fe/Zr (Ref. 31). On the other hand, trace amounts of Al, Si, and Mn in both 316L and Hastelloy-N generally produced a solid solution form in the coatings. However, the small amounts of the NiZrSi and Ni_2ZrAl phases that formed in the inner part of the coating on Hastelloy-N indicate that the Al and Si not only stayed in solid solution form but also accumulated in the coating. The reason that the accumulations of Al and Si in the coating were observed only on Hastelloy-N can be attributed to the greater Ni outward diffusion on Hastelloy-N, which left the Al-rich and Si-rich layers.

IV.D. Performance Speculation

The tendency for alloying constituents in 316L and Hastelloy-N to be attacked in molten fluoride salts increases in the following order: Ni, Fe, and Cr (Ref. 3). Addition of Zr to molten FLiNaK salt resulted in the formation of a coating containing mainly Zr and Ni, on the 316L and Hastelloy-N samples. This coating acts as a barrier layer by reducing the outward diffusion of Fe and Cr by the preferential movement of Ni. This effectively protects the substrate from further corrosion since Ni is relatively noble as well as the closest alloying constituent to the surface. However, the coatings on the 316L and Hastelloy-N are composed of Ni-Zr intermetallic phases, which are more brittle than the metallic substrate. Also, the thermal expansion coefficient mismatch between the coating and the substrate can result in cracking in the coating when the samples undergo thermal shock or thermal cycling.[32] Thus, the thin coating on 316L could provide a better corrosion resistance than the thicker coating on Hastelloy-N.

Graphite sustained structural damage in all test scenarios due to cascading interactions between Zr and oxygen. This effect is of concern for reactor designs that incorporate graphite as a major core component. An obvious potential solution to limiting the extent of graphite damage is to curb the ingress of oxygen through the development of salt purification processes and through careful salt-handling practices. On the other hand, the relatively small surface area of graphite contained in this test compared to a realistic reactor environment may diminish the potency of the eroding effect to such an extent that it is no longer a concern.

V. CONCLUSIONS

The effect of Zr addition on the corrosion behavior of 316L and Hastelloy-N in molten FLiNaK salt was investigated by static corrosion tests at 850°C for 1000 h. Addition of Zr drastically changed the corrosion behavior of 316L and Hastelloy-N in the molten salt by the deposition of a Zr coating, which subsequently formed a Zr-Ni intermetallic compound coating due to the outward diffusion of Ni in the substrate. The coating on Hastelloy-N had a larger thickness than the coating on 316L, which can be explained by the greater Zr deposition on Hastelloy-N due to the larger EMP difference between Ni/Zr compared to Fe/Zr. The Zr_3NiO and ZrO_2 phases were observed on the coating surfaces and in the coatings, respectively. The formation of Zr_3NiO and ZrO_2 may be the result of H_2O impurity in the molten salt. Graphite decreased the number and size of the ZrO_2 particles in the coatings but had no significant effect on the formation of the coatings. Thus, the corrosion resistance of 316L and Hastelloy-N to molten FLiNaK salt can be enhanced by the in situ formation of Ni-Zr coatings because the coatings can act as a barrier layer for Fe and Cr outward diffusion.

ACKNOWLEDGMENTS

The authors are very grateful to the U.S. Department of Energy for funding support under grants DOE-FC07-05ID14675 and DOE-FC07-07ID14826. This research utilized National Science Foundation–supported shared facilities at the University of Wisconsin.

REFERENCES

1. D. F. WILLIAMS, "Assessment of Candidate Molten Salt Coolants for the NGNP/NHI Heat-Transfer Loop," ORNL/TM-2006/69, Oak Ridge National Laboratory (2006).

2. D. WILLIAMS, L. TOTH, and K. CLARNO, "Assessment of Candidate Molten Salt Coolants for the Advanced High-Temperature Reactor (AHTR)," ORNL/TM-2006/12, Oak Ridge National Laboratory (2006).

3. L. C. OLSON et al., "Materials Corrosion in Molten LiF-NaF-KF Salt," *J. Fluorine Chem.*, **130**, 67 (2009).

4. M. KONDO et al., "Corrosion Characteristics of Reduced Activation Ferritic Steel, JLF-1 (8.92Cr–2W) in Molten Salts Flibe and Flinak," *Fusion Eng. Des.*, **84**, 1081 (2009).

5. M. KONDO et al., "Corrosion of Reduced Activation Ferritic Martensitic Steel JLF-1 in Purified Flinak at Static and Flowing Conditions," *Fusion Eng. Des.*, **85**, 1430 (2010).

6. M. S. SOHAL et al., "Engineering Database of Liquid Salt Thermophysical and Thermochemical Properties," INL/EXT-10-18297, Idaho National Laboratory (2010).

7. S. G. HONG and S. B. LEE, "The Tensile and Low-Cycle Fatigue Behavior of Cold Worked 316L Stainless Steel: Influence of Dynamic Strain Aging," *Int. J. Fatigue*, **26**, 899 (2004).

8. W. R. GRIMES et al., "Chemical Aspects of Molten Fluoride Salt Reactor Fuels," *Fluid-Fueled Reactors*, p. 569, Addison-Wesley (1958).

9. R. B. BRIGGS, "Molten-Salt Reactor Program Semiannual Progress Report for Period Ending July 31, 1964," ORNL/TM-3708, Oak Ridge National Laboratory (1964).

10. R. HURST and R. N. LYON, "Series IV: Technology, Engineering and Safety," *Progress in Nuclear Energy*, Vol. 2, p. 164, C. M. NICHOLLS, Ed. (1960).

11. J. H. SHAFFER, "Preparation and Handling of Salt Mixtures for the Molten Salt Reactor Experiment," ORNL/TM-4616, Oak Ridge National Laboratory (1971).

12. J. R. KEISER, J. H. DEVAN, and D. L. MANNING, "The Corrosion Resistance of Type 316 Stainless Steel to Li_2BeF_4," ORNL/TM-5782, Oak Ridge National Laboratory (1977).

13. G. D. DEL CUL et al., "Redox Potential of Novel Electrochemical Buffers Useful for Corrosion Prevention in Molten Fluorides," *Proc. 13th Int. Symp. Molten Salts*, Philadelphia, Pennsylvania, 2002, p. 12 (2002).

14. D. OLANDER, "Redox Condition in Molten Fluoride Salts Definition and Control," *J. Nucl. Mater.*, **300**, 270 (2002).

15. V. RAGHAVAN, "The Fe-Ni-Zr (Iron-Nickel-Zirconium) System, Phase Diagrams Ternary Iron Alloys," *Indian Inst. Met.*, **6B**, 1094 (1992).

16. D. B. ABRAHAM, J. W. RICHARDSON, and S. M. McDEAVITT, "Microscopy and Neutron Diffraction Study of a Zirconium-8 wt% Stainless Steel Alloy," *J. Mater. Sci.*, **36**, 5143 (2001).

17. G. GHOSH, "Thermodynamics and Kinetics of Stable and Metastable Phases in the Ni–Zr System," *J. Mater. Res.*, **9**, 598 (1994).

18. C. WANG, M. ZINKEVICH, and F. ALDINGER, "On the Thermodynamic Modeling of the Zr-O System," *Calphad*, **28**, 281 (2004).

19. J. GOLCZEWSKI et al., "Phase Diagrams of the Ni-Fe-Mo and Ni-Cr-Mo Ternary Systems—Experiments and Thermodynamic Calculations as a Basis of Superalloy Development," *Proc. 1st European Conf. Advanced Materials and Processes (EUROMAT'89)*, Aachen, Germany, 1989, Vol. 1, p. 365 (1989).

20. G. GHOSH, "Aluminium-Nickel-Zirconium," *Ternary Alloys*, p. 71, Wiley-VCH (1992).

21. Y. V. VOROSHILOV, V. Y. MARKIV, and E. GLADYSHEVSKII, "The Zirconium-Nickel-Silicon System," *Inorg. Mater.*, **3**, 1224 (1967).

22. G. KIPOUROS and S. FLENGAS, "Electrorefining of Zirconium Metal in Alkali Chloride and Alkali Fluoride Fused Electrolytes," *J. Electrochem. Soc.*, **132**, 1087 (1985).

23. H. GROULT et al., "Study of the Electrochemical Reduction of Zr^{4+} Ions in Molten Alkali Fluorides," *J. Electrochem. Soc.*, **155**, E19 (2008).

24. A. GIRGINOV, T. TZVETKOFF, and M. BOJINOV, "Electrodeposition of Refractory Metals (Ti, Zr, Nb, Ta) from Molten Salt Electrolytes," *J. Appl. Electrochem.*, **25**, 993 (1995).

25. G. W. MELLORS and S. SENDEROFF, "Electrode Reactions in the Electrolysis of Fused Salts," *Proc. 1st Conf. Thermodynamic Properties of Materials—Applications of Fundamental Thermodynamics to Metallurgical Processes*, Pittsburgh, Pennsylvania, 1967, p. 81 (1967).

26. L. GAL-OR, I. SILBERMAN, and R. CHAIM, "Electrolytic ZrO_2 Coatings," *J. Electrochem. Soc.*, **138**, 1939 (1991).

27. F. HOU, W. WANG, and H. GUO, "Effect of the Dispersibility of ZrO_2 Nanoparticles in Ni-ZrO_2 Electroplated Nanocomposite Coatings on the Mechanical Properties of Nanocomposite Coatings," *Appl. Surf. Sci.*, **252**, 3812 (2006).

28. I. N. OZERYANAYA et al., "Effect of Container Material on Reaction of Zirconium with Molten Strontium Chloride," *Tr. Inst. Elektrokhim., Ural. Nauch. Tsentr. Akad. Nauk SSSR*, 86 (1973).

29. D. DEVILLIERS et al., "Mass Spectrometric Analysis of Thermal Decomposition Products of Graphite Fluorides and Electrogenerated Carbon—Fluorine Compounds," *Anal. Chim. Acta.*, **153**, 69 (1983).

30. R. S. SELLERS et al., "Materials Corrosion in Molten LiF-NaF-KF Eutectic Salt Under Different Reduction-Oxidation Conditions," *Proc. Int. Conf. Advances in Nuclear Power Plants (ICAPP '12)*, Chicago, Illinois, June 24–28, 2012, American Nuclear Society (2012).

31. K. BHANUMURTHY, G. B. KALE, and S. K. KHERA, "Reaction Diffusion in the Zirconium-Iron System," *J. Nucl. Mater.*, **185**, 208 (1991).

32. Y. ZHANG et al., "Effect of Cycle Length on the Oxidation Performance of Iron Aluminide Coatings," *Surf. Coat. Technol.*, **188**, 35 (2004).